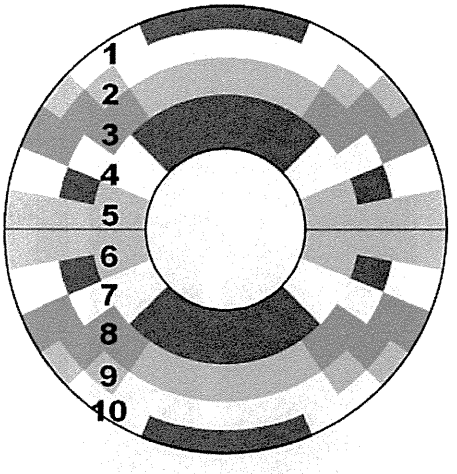

Fig. 1. Diagram of transducer element combination pattern.

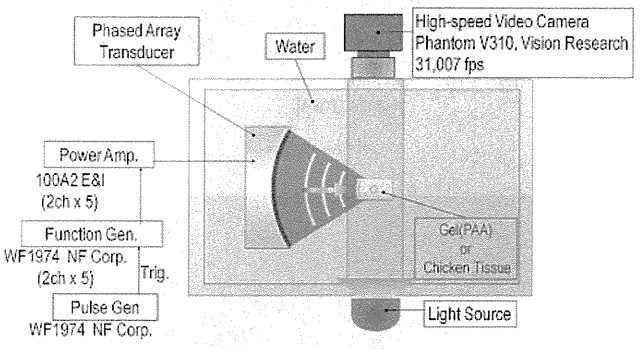

Fig. 2. Overall experiment setup.

1–10 from top to bottom. The elements in black were not driven. Observation of cavitation clouds in polyacrylamide (PAA) gel with a high-speed video camera and a thermal coagulation experiment with excised chicken breast tissue were performed with the transducer in degassed water [dissolved oxygen (DO) 30–40%, 22.0 °C]. The geometrical focal point, which is formed by driving each transducer element at the same phase, was located at a depth of 10 mm from the surface of the PAA gel and chicken breast tissue. The behavior of cavitation clouds was recorded using a high-speed video camera (Vision Research Phantom V310). The framing rate of the camera was 31,007 fps, the exposure time was 1 μs, and the resolution was 320×240. The gel around the focal point was illuminated from the direction perpendicular to the ultrasonic propagation axis. The experimental setup is shown in Fig. 2.

2.2 Tissue-mimicking phantom preparation[22)]

We generated an optically transparent tissue-mimicking phantom based on polyacrylamide gel. Its air content was controlled by adjusting the time and pressure of degassing during gel formation.

The following protocol for phantom fabrication was used: degassed, distilled water at a concentration of 70% (v/v) and 1 M tris(hydroxymethyl)aminomethane (TRIS) buffer (Sigma Aldrich T1378) adjusted to pH 8 with 1 M HCl

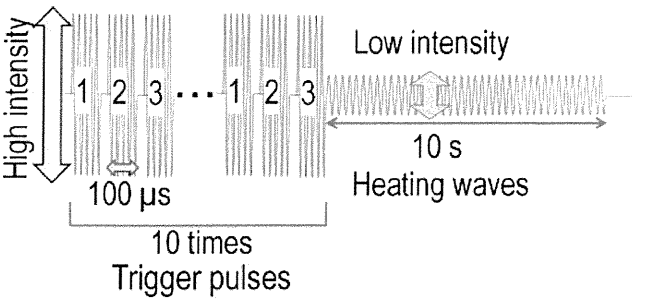

Fig. 3. Schematic of ultrasound sequence to produce multiple coagulation spots simultaneously.

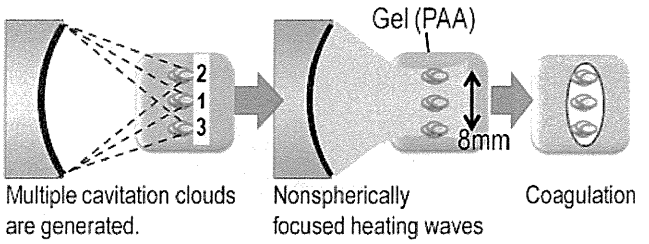

Fig. 4. Schematics of proposed ultrasound sequence with gel phantom.

(Kanto Chemical 18591-08) at a concentration of 9.2% (v/v) were mixed and used to dissolve the bovine serum albumin (BSA; Sigma Aldrich A7906) at a concentration of 10% (w/v). The solution was gently stirred to mix the BSA powder. 40% (w/v) acrylamide solution (Sigma Aldrich A7186, 37.5:1) was mixed with the solution at a concentration of 20% (v/v). The solution was degassed at 10 kPa for 1 h. The polymerization was initiated by adding a 20% ammonium persulfate solution (APS; Sigma Aldrich A3678) at a concentration of 0.6% (v/v) and *N*,*N*,*N*′,*N*′-tetramethylethylene-diamine (TEMED; Sigma Aldrich T9281) at a concentration of 0.2% (v/v) at room temperature. The gels were air-tight-sealed in plastic bags, stored at 6 to 10 °C, and used the next day. The air content in the gel was not directly measured because no effective method was available.

2.3 Ultrasound sequence

The ultrasound sequence in this experiment and the corresponding phenomenon in the focal region are shown in Figs. 3 and 4, respectively. It is known that cavitation clouds are generated by a significant negative pressure in the focal region of HIFU. First, cavitation clouds were generated at $x = 0$, -4, and $+4$ mm (1, 2, and 3, respectively, in Fig. 3) by changing the driving phases of the combined groups of elements, where the x-axis is perpendicular to the direction of ultrasound propagation with its origin at the geometrical focal point. Immediately after that, a relatively low intensity ultrasound that cannot coagulate either the gel or the tissue by itself was irradiated with an enlarged focus covering all the three focal positions before the extinction of the cavitation clouds. The oscillation of cavitation bubbles may enhance the tissue heating, and coagulation regions may be generated.

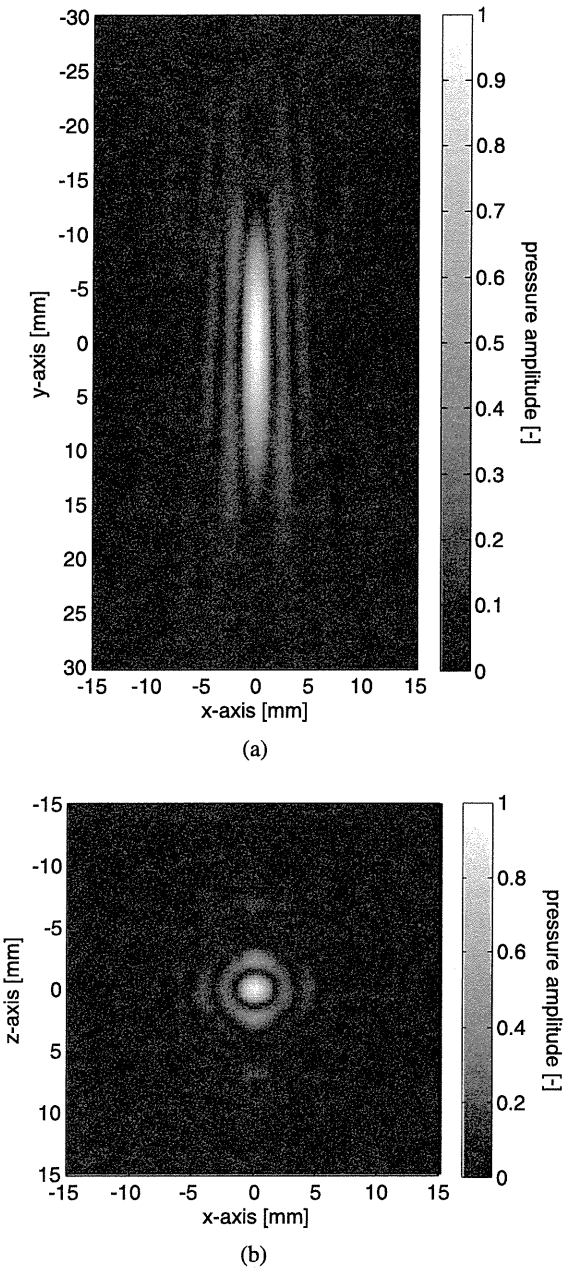

Fig. 5. Numerical result of trigger pulse pressure field, when focused at $x = 0$, in (a) x–y and (b) x–z planes.

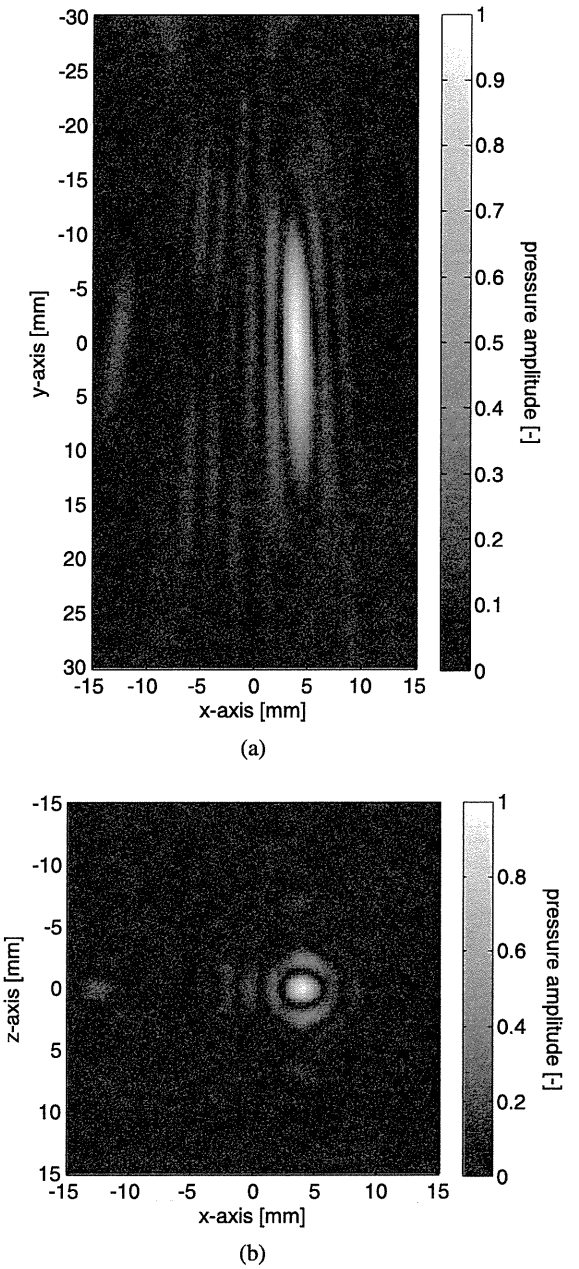

Fig. 6. Numerical result of trigger pulse pressure field, when focused at $x = 4$ mm, in (a) x–y and (b) x–z planes.

2.4 Trigger pulse

A trigger pulse focused onto each focal point was irradiated for 100 μs. The focal pressure field was numerically calculated by linear approximation and the normalized root-mean-square amplitude is shown in Figs. 5 and 6, where point (0, 0) is the geometric focal point of the transducer and the positive direction on the y-axis is the direction of ultrasound propagation. The focal point was located at $x = 0$ and 4 mm in Figs. 5 and 6, respectively. It was sequentially varied at $x = 0$ and ±4 mm by changing the phase of the output waves from the multifunction generators. The cycle of trigger pulses, sequentially focused onto each one of the three focal points, was repeated 10 times at a repetition frequency of 3.3 kHz. It was repeated in order to increase the probability of generating cavitation clouds. The total irradiation time was 1.0 ms for each focal point. The phases of the waves from each element are listed in Table I for the focal point at $x = +4$ mm. The phases for $x = -4$ mm are their inversion phases. The spatial-peak temporal-peak intensities (I_{SPTP}) at each focal point were 32 kW/cm^2 produced at the maximum output power of the RF amplifiers. The phases of the waves from each element were calculated from the distance between the element and the focal point. The ultrasonic intensity was calculated from the measurement of the acoustic pressure with a hydrophone (ONDA HGL-0085) in water. The intensity of the trigger pulses and the following heating waves was estimated by measuring it at an intensity of 12.4 W/cm^2 by assuming a quadratic relation between the amplifier output voltage and the intensity.

Table I. Ultrasound phases and amplitudes of each element for focal point at $x = +4$ mm and for nonspherically focus of heating waves.

Element	+4 mm		Nonspherical focusing	
	Amplitude	Phase (deg)	Amplitude	Phase (deg)
1	1.000	126.7	0.391	155.5
2	1.000	197.0	0.217	97.2
3	1.000	277.0	1.000	1.1
4	1.000	7.7	1.000	0.0
5	1.000	96.9	0.304	125.2
6	1.000	178.1	0.304	125.2
7	1.000	267.9	1.000	0.0
8	1.000	0.0	1.000	1.1
9	1.000	81.7	0.217	97.2
10	1.000	154.0	0.391	155.5

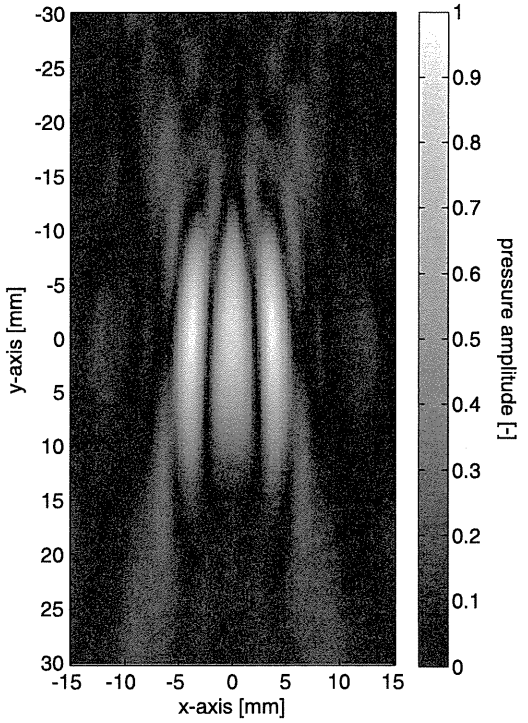

Fig. 7. Numerical result of heating wave pressure field in x–y plane.

2.5 Heating waves

The driving phases and amplitudes of elements for nonspherical focusing were obtained by time reversal. A point source with equal strength was located on each of the three target positions, and the time-reversed ultrasound was received by each transducer element. The received signals were averaged in each element group, time-reversed, and sent again to form a nonspherical focal field. The phase of each point source was optimized to equalize the acoustic pressure on the three points. The focal pressure field was numerically calculated by linear approximation and the normalized amplitude is shown in Figs. 7 and 8. The root-mean-square amplitude is shown in Figs. 7 and 8(a), and the instantaneous amplitude is shown in Fig. 8(b). Note that the side foci in the negative and positive x-axes have the same absolute amplitude as the central focus but opposite sign. The driving phases and amplitudes of elements are also

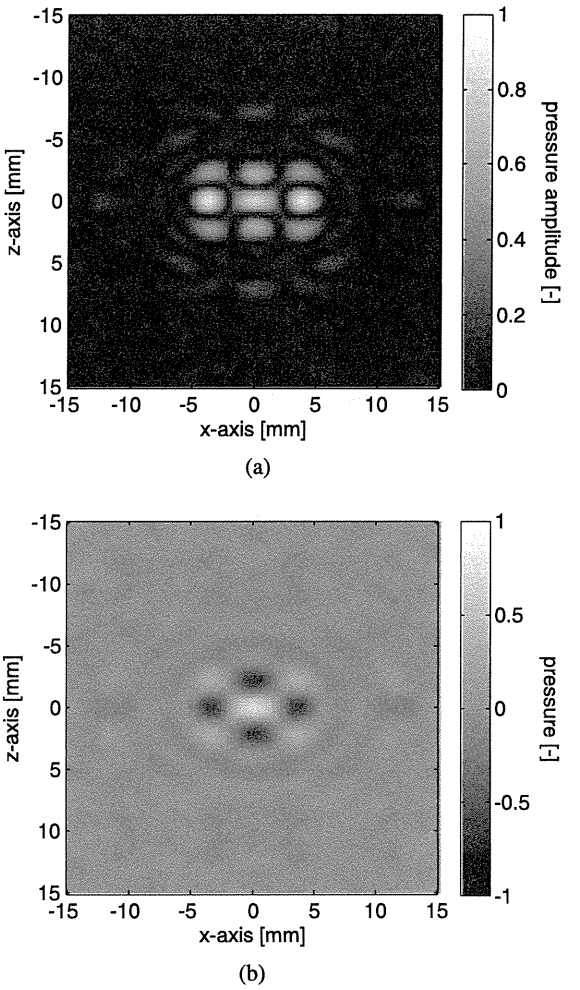

Fig. 8. Numerical result of heating wave pressure field in x–z plane. (a) Root-mean-square pressure and (b) instantaneous acoustic pressure.

shown in Table I. The spatial-peak temporal-average intensities (I_{SPTA}) were 600, 800, and 900 W/cm^2 and the exposure time was 10 s.

3. Results

3.1 Observation of cavitation clouds

The behaviors of cavitation clouds in a gel phantom are shown in Fig. 9. The arrow in each frame shows the lateral position of the focal point of the trigger pulse. At 0 μs, the first trigger pulse reaches the focal point. At $x = 0$ mm, a small cavitated bubble is generated at 98 μs in the first trigger cycle; it grows to a cavitation cloud in a moderate to large size at 322 to 354 μs in the second cycle. At $x = -4$ mm, a cavitation cloud is generated at 194 μs; it grows to a considerable size at 226 μs in the first cycle. It grows to a large size at 418 and 450 μs in the second cycle. At $x = +4$ mm, a small cavitated bubble is generated at 1419 μs; it grows to a large cavitation cloud at 1505 μs in the fifth triggering cycle. At 3031 μs and 6.4 ms, cavitation clouds during the heating waves are seen.

High-speed camera observation of the behavior of cavitation clouds, although not applicable to *in vivo* observation, demonstrated its usefulness owing to its spatial resolution much higher than acoustical methods such as subharmonic detection.

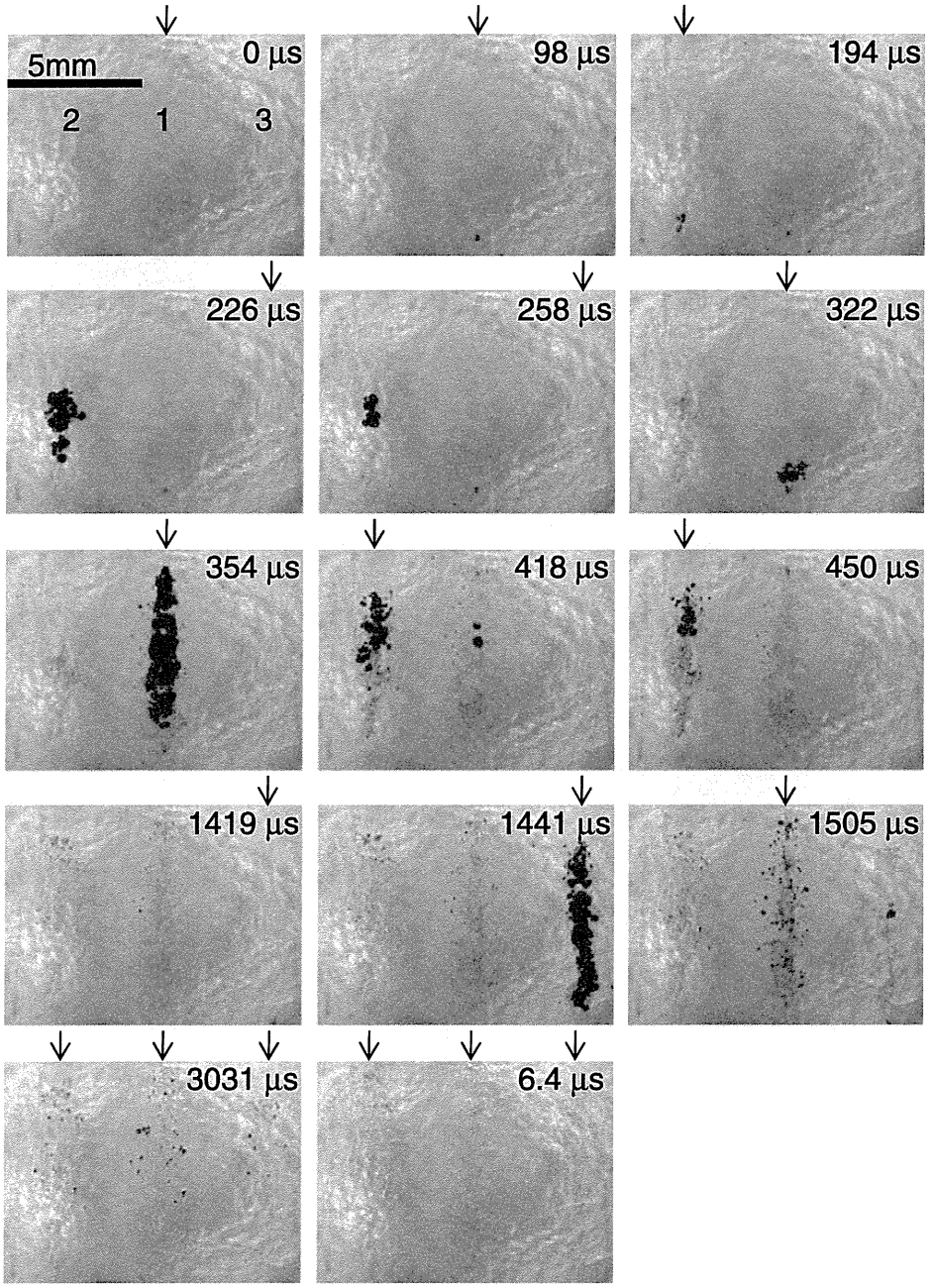

Fig. 9. Optical change in gel phantom during the ultrasound sequence. First trigger pulse focused onto the geometrical focal point at $t = 0$. The numbers in the first picture correspond to the focal positions of the trigger pulses shown in Fig. 4. The arrows indicate the lateral focal positions of the trigger pulse or heating waves.

3.2 Coagulation region

The result of the coagulation experiment using chicken tissue with triggered HIFU is shown in Fig. 10. Figures 10(a), 10(b), and 10(c) show coagulation with trigger pulses and Figs. 10(a′), 10(b′), and 10(c′) show coagulation without trigger pulses. The intensities of heating waves were 600 W/cm^2 for Figs. 10(a) and 10(a′), 800 W/cm^2 for Figs. 10(b) and 10(b′), and 900 W/cm^2 for Figs. 10(c) and 10(c′). These intensities were optimized by determining the intensity at which the tissue around the side foci of the heating waves did not coagulate without trigger pulses. The region of coagulation with trigger pulses was larger than the coagulation region without those. In addition, the coagulation region with trigger pulses was enlarged by merging that of each focal point by increasing the intensity of heating waves.

4. Discussion

For the reproducible efficiency of the sequence utilizing cavitation clouds, the following three points are important. 1) Cavitation clouds should be generated at objective positions by trigger pulses. 2) The generated cavitation clouds should survive until heating waves reach them. 3) Heating waves should cover all cavitation clouds. These were confirmed by observing the behavior of cavitation clouds in a gel phantom with a high-speed camera.

In the experiment, cavitation clouds were generated at $x = 0$, -4, and $+4$ mm in sequence. This sequence has been

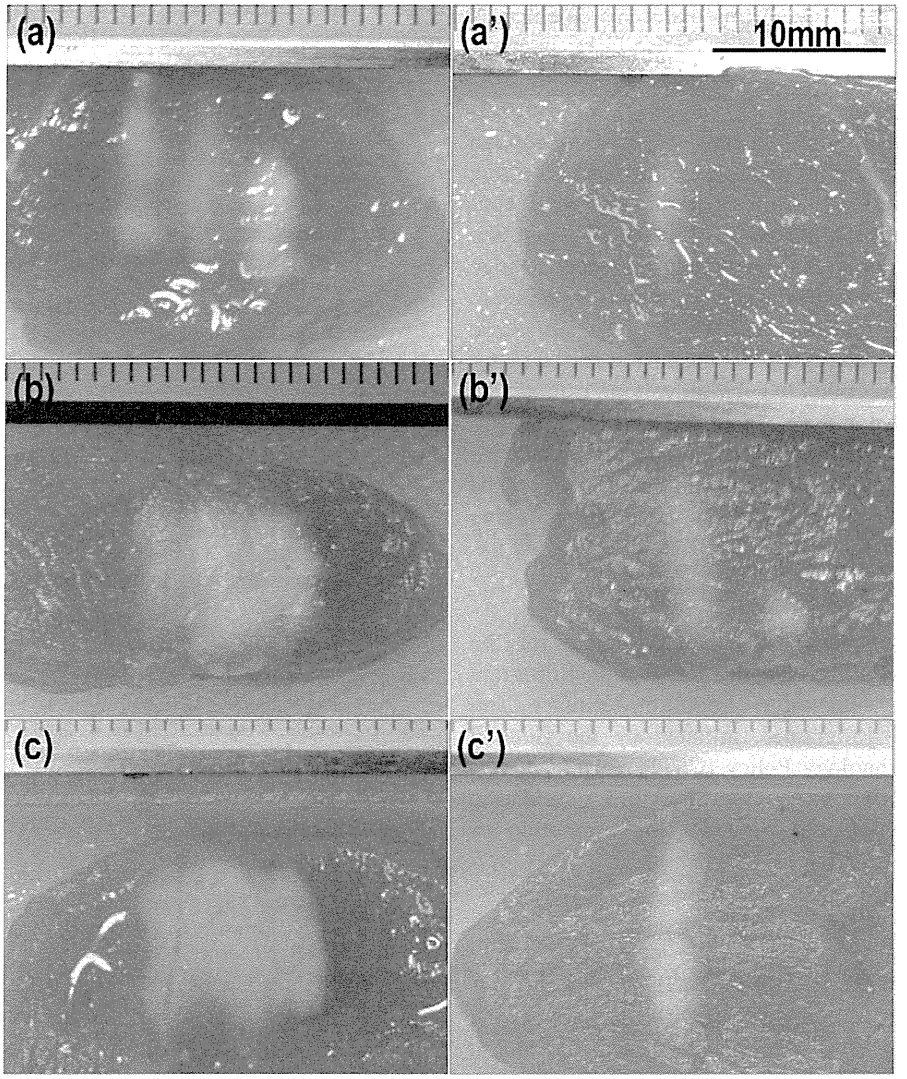

Fig. 10. Chicken breast tissue coagulated using the ultrasound sequence.

chosen by considering the nature of a bubble as an acoustic reflector and the effect of the side lobes of a steered focal beam to help sustain cavitation clouds, but it may be optimized with further study. The result in Fig. 9 indicates that the probability of generating cavitation clouds can be increased by repeating the cycle of trigger pulses and that the chosen sequence of trigger pulse is reasonable.

The driving phases and amplitudes of the transducer elements for focusing the heating waves were obtained by time reversal. The applied time reversal focusing algorithm described in the clause 2.5 could generate the optimum driving phases and amplitudes.

At a low ultrasonic intensity, the tissue coagulated separately at each one of the three focal spots because ultrasonic power was not sufficient to coagulate the tissue between the neighboring focal spots through thermal conduction. The volume of each coaguled spot was about the same because the tissue around a cavitation cloud was nearly uniformly heated. By increasing the intensity or exposure time of heating waves, each of the coagulated spots increased its size to merge together. Without trigger pulses, the tissue coagulated at only one focal spot at $x = 0$ mm. From the other two outer focal spots, the heat diffused outward probably as a result of too high a thermal conductance. To coagulate the same volume of tissue without trigger pulses as with trigger pulses, the ultrasonic power of heating waves may have to be increased by approximately twofold.

In this study, much higher intensities of trigger pulses were used and larger volume of tissue than used in the last study[12] was coagulated at similar heating wave intensities. Although the coagulated volume in the last paper was only a small portion of the heating focal volume enlarged parallel to the direction of ultrasound propagation, that in this study was a major portion of the heating focal volume enlarged perpendicular to the direction of ultrasound propagation. This is probably because a larger volume of cavitation clouds enhancing ultrasonic absorption was formed at a higher reproducibility. The improvement in heating efficiency due to the change in the direction of focus control may also have contributed to the production of a larger coagulation volume.

The results of the coagulation experiments in this study in addition to that of the last study proved that this triggered HIFU approach is useful to enlarge the coagulation volume in the direction perpendicular as well as parallel to

ultrasound propagation,[12] suggesting that it can be enlarged three dimensionally if needed.

5. Conclusions

The roles of multiple high-intensity cavitation-inception pulses and nonspherically focused heating waves in forming an enlarged coagulation volume reproducibly were confirmed by observing the behavior of incepted cavitation clouds in a tissue-mimicking gel with a high-speed video camera as well as by excised tissue coagulation experiment. The result suggested that the total length of the ultrasonic exposure sequence needed can be reduced by at least a factor of three because a threefold coagulation volume is produced by one heating wave burst at a lower ultrasonic power, therefore requiring a shorter cooling interval between bursts than that used in conventional HIFU treatment. HIFU treatment time will be significantly shortened by employing the proposed method.

Acknowledgments

This research is granted by the Japan Society for the Promotion of Science (JSPS) through the "Funding Program for World-Leading Innovative R&D on Science and Technology (FIRST Program)", initiated by the Council for Science and Technology Policy (CSTP). A part of this research was supported by a Grant-in-Aid for Scientific Research from the Japan Society for the Promotion of Science (JSPS).

1) M. Malinen, T. Huttunen, J. P. Kaipio, and K. Hynynen: Phys. Med. Biol. **50** (2005) 3473.
2) V. Rouffiac, J.-S. Duret, P. Péronneau, N. Dehez, P. Opolon, A. Roche, and N. Lassau: Ultrasound Med. Biol. **32** (2006) 729.
3) T. Uchida, S. Shoji, M. Nakano, S. Hongo, M. Nitta, A. Murota, and Y. Nagata: Int. J. Urol. **16** (2009) 881.
4) T. Uchida, N. T. Sanghvi, T. A. Gardner, M. O. Koch, D. Ishii, S. Minei, T. Satoh, T. Hyodo, A. Irie, and S. Baba: Urology **59** (2002) 394.
5) K. Numata, H. Fukuda, M. Ohto, R. Itou, A. Nozaki, M. Kondou, M. Morimoto, E. Karasawa, and K. Tanaka: to be published in Eur. J. Radiol. [DOI: 10.1016/j.ejrad.2009.11.022].
6) S. Umemura and K. Sasaki: Proc. IEEE Ultrasonics Symp., 1999, p. 1409.
7) K. Kawabata and S. Umemura: Jpn. J. Appl. Phys. **42** (2003) 3246.
8) K. Kawabata, N. Sugita, H. Yoshikawa, T. Azuma, and S. Umemura: Jpn. J. Appl. Phys. **44** (2005) 4548.
9) S. Umemura, K. Kawabata, and K. Sasaki: IEEE Trans. Ultrason. Ferroelectr. Freq. Control **52** (2005) 1690.
10) L. A. Frizzell: in *Ultrasound*, ed. K. S. Suslick (Wiley/VCH, Weinheim, 1988) Chap. 4, p. 287.
11) R. Takagi, S. Yoshizawa, and S. Umemura: Jpn. J. Appl. Phys. **49** (2010) 07HF21.
12) Y. Inaba, S. Yoshizawa, and S. Umemura: Jpn. J. Appl. Phys. **49** (2010) 07HF22.
13) Z. Xu, M. Raghavan, T. L. Hall, C. W. Chang, M. A. Mycek, J. B. Fowlkes, and C. A. Cain: IEEE Trans. Ultrason. Ferroelectr. Freq. Control **54** (2007) 2091.
14) S. Umemura and C. A. Cain: IEEE Trans. Ultrason. Ferroelectr. Freq. Control **36** (1989) 249.
15) E. S. Ebbini: IEEE Trans. Ultrason. Ferroelectr. Freq. Control **36** (1989) 540.
16) K. Sasaki, T. Azuma, K. Kawabata, M. Shimada, E. Kokue, and S. Umemura: Ultrasound Med. Biol. **29** (2003) 591.
17) S. Umemura, T. Azuma, Y. Miwa, K. Sasaki, T. Sugiyama, T. Hayashi, and H. Kuribara: Proc. IEEE Ultrasonics Symp., 2002, p. 1721.
18) D. A. Guenther and W. F. Walker: IEEE Trans. Ultrason. Ferroelectr. Freq. Control **54** (2007) 332.
19) M. Yamamoto, T. Azuma, and S. Umemura: Jpn. J. Appl. Phys. **48** (2009) 07GJ03.
20) T. R. Gururaja, W. A. Schulze, L. E. Cross, R. E. Newnham, B. A. Auld, and Y. J. Wang: IEEE Trans. Sonics Ultrason. **32** (1985) 481.
21) G. Fleury, R. Berriet, O. Le Baron, and B. Huguenin: Proc. 2nd Int. Symp. Therapeutic Ultrasound, 2002, p. 428.
22) C. Lafon, V. Zderic, M. L. Noble, J. C. Yuen, P. J. Kaczkowski, O. A. Sapozhnikov, F. Chavrier, L. A. Crum, and S. Vaezy: Ultrasound Med. Biol. **31** (2005) 1383.

Displays 32 (2011) 201–208

Contents lists available at ScienceDirect

Displays

journal homepage: www.elsevier.com/locate/displa

Evaluation of temporal relationship between a physiological index and a subjective score using average mutual information

Norihiro Sugita [a,*], Makoto Yoshizawa [b], Akira Tanaka [c], Makoto Abe [b], Noriyasu Homma [b], Shigeru Chiba [d], Tomoyuki Yambe [e], Shin-ichi Nitta [e]

[a] Graduate School of Engineering, Tohoku University, 6-6-05 Aoba, Aramaki, Aoba-ku, Sendai 980-8579, Japan
[b] Information Synergy Center, Tohoku University, 6-6-05 Aoba, Aramaki, Aoba-ku, Sendai 980-8579, Japan
[c] Faculty of Symbiotic Systems Science, Fukushima University, 1 Kanayagawa, Fukushima 960-1296, Japan
[d] Sharp Corporation, 1-9-2 Nakase, Mihama-ku, Chiba 261-8520, Japan
[e] Institute of Development, Aging and Cancer, Tohoku University, 4-1 Seiryo-machi, Aoba-ku, Sendai 980-8575, Japan

ARTICLE INFO

Article history:
Available online 15 May 2011

Keywords:
Visually-induced motion sickness
Physiological index
Subjective score
Averaged mutual information

ABSTRACT

Recently, because of the ubiquitous popularization of home video cameras, countless people have had opportunities to watch video images captured by amateur cameramen. Because of this, concerns have arisen over potential negative impacts on viewer health, such as visually-induced motion sickness (VIMS). To determine the mechanism inducing VIMS and to establish a method of preventing it, it is necessary to understand which types of video scenes are associated with the onset of VIMS. Furthermore, while it is useful to consider viewer self-assessments while watching such scenes, physiological indices can provide even more information because they can be measured second-by-second in real time. However, there is not much knowledge regarding the temporal relationships between the severity of VIMS and its accompanying physiological conditions. In this study, the average mutual information was employed to determine the temporal relationship between subjective evaluation scores (a subject's personal evaluation of his/her own condition) and various physiological indices present when people suffer from VIMS. Our analysis of experimental data found that changes in the two physiological indices, which were respiratory sinus arrhythmia and the maximum cross-correlation coefficient between heart rate and pulse transmission time, had a concordance rate of more than 60% with changes in the severity of VIMS symptoms experienced by test subjects. Furthermore, we determined that it may be possible to detect signs of impending VIMS prior to the development of symptoms by analyzing physiological indices.

1. Introduction

In recent years, countless people have seen moving video images taken by amateur videographers. As a consequence, video cameras have become significantly less expensive and because the popular trend of posting private videos on the Internet has expanded exponentially. Concurrently, the number of cases reported in which viewers suffered from visually-induced motion sickness (VIMS) during or after watching a video, including unexpected whole image motion and vibration [1–9], has increased. VIMS is a form of motion sickness that does not require the subject to experience motion. However, VIMS symptoms are similar to those of other motion sicknesses. Most notably, such symptoms include skin pallor, excessive perspiration, nausea, and vomiting. At a junior high school in Japan on July 10, 2003, an incident occurred in which 36 of 294 students were treated in a hospital after complaining of dizziness and nausea induced by watching a video taken by an amateur videographer with a swaying handheld camera [6]. Furthermore, several film distributors and video game producers have recently issued warnings to viewers or users about the possibility of experiencing VIMS from watching their videos or playing their games: a movie titled "Clover Field" released in 2008 was one such example.

A number of *hypotheses* and discussions about the pathogenesis of various forms of motion sickness, including VIMS [10–12], have been explored. Nevertheless, there is currently little understanding about adverse effects of VIMS on the human body. Accordingly, sufficient attention should be focused on dealing with moving images and scenes that have potential to induce VIMS, especially in the case of children, because their nervous systems are immature.

To isolate the VIMS induction mechanism and to establish a method of preventing it, it is important to understand which

* Corresponding author. Tel.: +81 22 7957130; fax: +81 22 2639163.
E-mail address: sugita@yoshizawa.ecei.tohoku.ac.jp (N. Sugita).

0141-9382/$ - see front matter © 2011 Elsevier B.V. All rights reserved.
doi:10.1016/j.displa.2011.04.003

scenes in a video are associated with the onset of VIMS. Self-assessment of VIMS by subjects at regular intervals is considered to be one of the most effective methods of detecting these scenes. In particular, Kennedy developed the Simulator Sickness Questionnaire (SSQ) [13] which has been used in many studies [14–17]. The SSQ contains 16 items to check the subject's physical disorder. The subject rates the degree of these items in four levels. Three subscales, i.e., nausea, oculomotor, and disorientation, are calculated on the basis of these items, and a total score is calculated with these subscales. In these scales, the nausea subscale or the total score is considered to be useful for evaluating the severity of VIMS. However, since SSQ results can normally only be obtained after a subject has watched a video, it is difficult to follow changes in VIMS severity over time. Furthermore, even if self-assessment is accomplished using an easier reporting method than SSQ, such as reporting symptoms via keyboard input or verbally, the very act of making such reports has the potential to distract subjects from the scene they are viewing, and thus modify the VIMS development.

In contrast, other previous studies [2–5,7,8,18–23] have reported that real-time monitoring of physiological indices is also useful for detecting and following the development of VIMS. Specifically, skin conductance [20,21] and gastric tachyarrhythmia [2,20,22] are considered to be particularly indicative of possible VIMS. Furthermore, physiological indices based on heart rate variability (HRV) such as variations in respiratory sinus arrhythmia (RSA) [10,11] have possibilities of detecting the development of VIMS. The indices obtained from HRV are associated with autonomic nervous activity. Fig. 1 shows an example of the power spectrum density of HRV. In this figure, the high frequency component corresponding to RSA includes parasympathetic nervous activity only while the low frequency component (LF_{HRV}) includes both sympathetic and parasympathetic nervous activities [24,25]. These physiological indices are susceptible to change when a person experiences VIMS because VIMS is considered to be a kind of the physical and emotional stress which disturbs autonomic nervous balance. We previously proposed a maximum cross-correlation coefficient (ρ_{max}) between heart rate and blood pressure and reported that this index decreased significantly when people suffered from VIMS [4]. ρ_{max} is considered to reflect baroreflex function which is influenced by autonomic nervous activity [26–28]. In addition, ρ_{max} which was calculated using pulse transmission time (PTT) [29] instead of blood pressure was also found to be useful when evaluating VIMS effects [3,5].

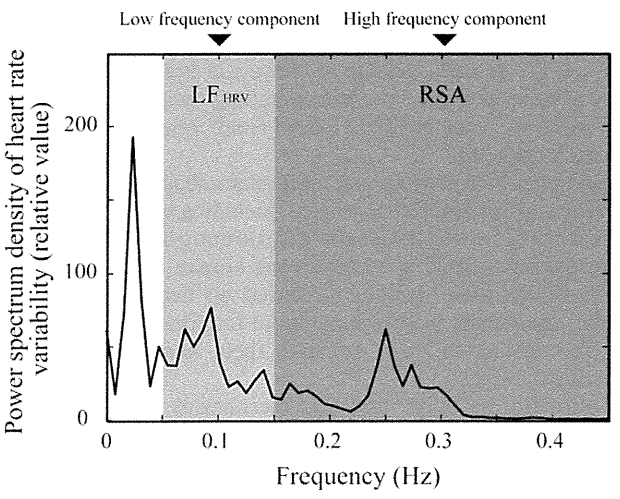

Fig. 1. The power spectrum density of heart rate variability.

Information on the abovementioned physiological indices can be obtained in real-time using non-invasive sensors while the subjects are watching a video, which makes it possible to compare changes in these indices with particular video scenes and thus observe the process of VIMS onset with relatively little effect on the subjects. However, one problem identified is that biological reaction times, especially response times, vary between individuals. Meanwhile, there have been few studies into the temporal relationship between the development of VIMS as evaluated by subjective scores and by the physiological responses of the subjects [19].

In this study, we hypothesize that there is no significant difference between the time when subjects experience VIMS symptoms and the time when their physiological states change. To test this hypothesis, an experiment was conducted to investigate the temporal relationship between a subjective score and four physiological indices, HRV, LF_{HRV}, RSA, and ρ_{max}, from subjects experiencing VIMS. It was not clear whether HRV and LF_{HRV} reflect the development of VIMS, although RSA and ρ_{max} were reported to have relationships with VIMS in previous works [3–5,18,19].

2. Methods

2.1. Experimental design

In the experimental phase of this study, both subjective scores and biological signals were measured simultaneously while subjects were watching a video. The test subjects evaluated the degrees of VIMS they experienced at regular intervals using a joystick. In contrast, physiological state changes, HRV, LF_{HRV}, RSA, and ρ_{max} using PTT were obtained via biological signals, and were used as physiological indices to test our hypothesis. Furthermore, we proposed a new evaluation indicator, which will be described in detail later, to investigate the temporal relationship between subjective scores and the physiological indices.

The experimental protocol was approved by the University's Internal Review Board.

2.2. Participants

Fifty-one adults (22 males and 29 females; 26.6 ± 9.3 years) participated in the experiment. They were recruited via posted announcements on university notice boards, and all of them received payment for their participation in the experiment.

Informed consent was obtained from each of the subjects and each was asked about their backgrounds and health conditions through a questionnaire. The results of the questionnaire showed that there were no test subjects whose participation in the experiment would be unsuitable due to health issues.

2.3. Stimulus

The subjects watched a 20-min-long amateur video that included three segments, as shown in Fig. 2. Segment one consisted of moving images taken by a young girl using a hand-held camera while strolling around an urban area. Therefore, the video contained numerous scenes that included unexpected whole image motions and vibration. The images of Segment 2 were taken in an amusement park. Thus, the camera movements were sometimes intense due to the movements of the theme-park rides. Segment 3 includes images of a young woman strolling around a city, recorded normally, and using four simple camera motions: tilt, pan, roll and zoom. Before and after these segments, a gray, imageless screen display was presented to the subjects for 5 min 30 s and 2 min, respectively. Therefore, each subject watched a total of 27 min 30 s of video during the experiment. None of the three vi-

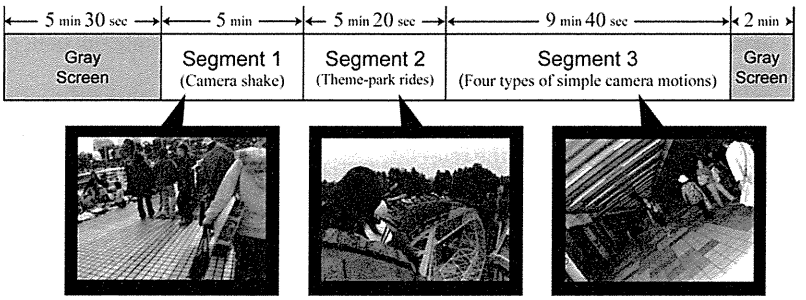

Fig. 2. Overview of the video presented to experimental subjects.

deo segments had story lines and there were no violent scenes that might induce emotional effects.

The global motion vectors (GMVs) of the video are shown in Fig. 6a). GMVs are measurements of deviation between consecutive frames and represent degrees of motions in four axes: pan, tilt, roll and zoom. A detailed description of the method used for estimating GMVs is provided in Ref. [30]. As shown in Fig. 6a, scenes with intense camera movements and those without were mixed in the video on purpose to induce ups and downs of VIMS symptoms.

2.4. Equipment

The video was shown on a 37-in. liquid crystal display (resolution: 1920 × 1080 pixels, maximum brightness: 200 cd/m^2). The experimental room had curtains that eliminated all outside light and illumination intensity was maintained at approximately 50 lx. The room temperature was controlled with an air conditioner to be approximately 22 °C.

During the experiment, an electrocardiogram (ECG) for RSA, PTT, and HRV was measured using electrodes placed on the subjects chests. In addition, a finger photoplethysmogram (PPG) for PTT was also measured using a photoplethysmographic sensor attached on their finger tips, as shown in Fig. 3. These signals were amplified and recorded by a data acquisition system (MP-100, ECG100C, PPG100C; BIOPAC System Inc.); whose voltage resolution and sampling rate were 16 bit and 1 kHz, respectively.

2.5. Procedure

The subjects were instructed not to engage in intense physical activity and to avoid eating anything for 2 h prior to the experiment.

First, each subject was asked to complete a questionnaire about their background and health condition. Additionally, an SSQ [13] was administered before and after the experimental task to measure their VIMS symptoms. Next, after being seated in the room and given 10 min to adapt to the darkness, they began viewing the video.

While watching the video, test subjects sat on a chair placed 70 cm away from the display with a 60.5 × 40.3° field of view, and they rated the level of nausea they felt on a scale of zero to three by moving a joystick, as shown in Fig. 4. The number of symptom levels was limited to four and enough time for practice was given to the subjects before the experiment so that they could move the joystick appropriately without looking at it. A buzzer was sounded at 1 min intervals to let the subjects know it was time to rate their nausea level.

2.6. Data analysis

There were five subjects who complained of VIMS symptoms that were so severe that they could not continue to watch the video. All these subjects experienced nausea and had unnatural skin pallor. One female test subject developed an erratic heartbeat just before the experiment was stopped. Additionally, test data from 17 other subjects were excluded from the analysis because of artifacts. There were a large number of subjects whose photoplethysmogram signals contained artifacts caused by body movements. As shown in Fig. 3, the photoplethysmographic sensor is attached to the skin on a finger of a subject and detects infrared light modulated by blood pulsing through the tissue below. Therefore, the photoplethysmogram signal is disturbed if the subject's upper body including fingers moves much. Furthermore, data from another six subjects whose subjective scores were zero through the video were also excluded from the analysis. The reason of this will be discussed later. As a result, only the data of 23 subjects (10 males and 13 females; 27.6 ± 10.0 years) were analyzed.

As previously mentioned, we proposed a new evaluation indicator to investigate the temporal relationship between subjective

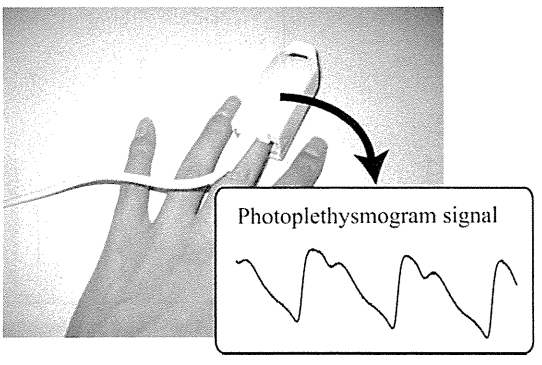

Fig. 3. Photoplethysmographic sensor attached on a subject's finger tips.

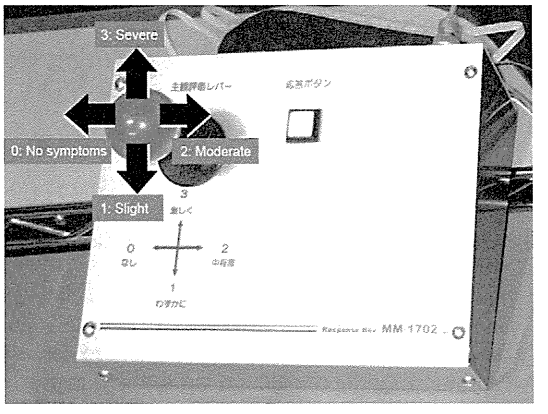

Fig. 4. Joystick used by subjects to rate VIMS symptoms during the experiment.

scores and physiological indices. In concrete terms, the average mutual information (AMI) [31] was calculated to measure the statistical dependence between the two. The AMI between two variables shows how frequently, on average, one of them can be estimated from the other. Thus, by introducing the AMI, it is possible to estimate the statistical dependence correctly even if the relationship between the variables is not linear. This property is important because our understanding of the linearity between subjective scores and physiological indices is still poor.

Problems sometimes occurred when calculating the AMI between subjective scores and physiological indices. Specifically, not only is the difference in the numeric resolution between them large, but the pattern of their changes differs significantly between individual subjects. To solve these problems, the AMI was calculated as the statistical dependence between events defined by changing patterns of variables, which were assessed as increasing, decreasing or stable.

We will further illustrate this point with an example utilizing two test subjects. In this example, when the subjective scores of the two subjects increase, the physiological index of one subject always increases while that of the other always decreases, and vice versa. In this situation, a difference appears in the value of an AMI calculated directly from the physiological index and the subjective scores of the two subjects. In contrast, the value of an AMI calculated based on events defined by changing patterns of the physiological index and the subjective scores of the two subjects is the same. Types of VIMS symptoms should differ among subjects, for example, eye fatigue, a headache or stomach discomfort. And autonomic nervous activities are supposed to vary in these different symptoms. For this reason, it is no wonder if directions of the change in physiological indices differ among the subjects when they suffered from VIMS. Additionally, the problem caused by the numerical differences between the two variables is also eliminated by simply comparing their changing patterns.

The method used to calculate the AMI will now be described in detail. First, events A_1, A_2, A_3 and B_1, B_2, B_3 are defined as follows:

$$\begin{aligned} A_1 &\Longleftrightarrow SS(k) - SS(k-1) > 0 \\ A_2 &\Longleftrightarrow SS(k) - SS(k-1) = 0 \\ A_3 &\Longleftrightarrow SS(k) - SS(k-1) < 0 \end{aligned} \tag{1}$$

$$\begin{aligned} B_1 &\Longleftrightarrow \frac{PS(k)}{PS(k-1)} > 1 + Tr \\ B2 &\Longleftrightarrow 1 - Tr < \frac{PS(k)}{PS(k-1)} \leqslant 1 + Tr \\ B3 &\Longleftrightarrow \frac{PS(k)}{PS(k-1)} \leqslant 1 - Tr \end{aligned} \tag{2}$$

where $SS(k)$ and $PS(k)$ are the subjective score and the physiological index at a given time k, respectively, and Tr is the threshold. A method to determine Tr is described later.

Next, the AMI between A_i and B_j (i, $j = 1,2,3$) is defined as follows:

$$I(A_i; B_j) = -\sum_{i=1}^{3} P(A_i)\log_2 P(A_i) + \sum_{i=1}^{3}\sum_{j=1}^{3} P(A_i, B_j)\log_2 P(A_i|B_j) \tag{3}$$

where $P(A_i)$ is the occurrence probability of A_i, $P(A_i, B_j)$ is the joint probability of A_i and B_j, and $P(A_i|B_j)$ is the conditional probability of A_i assuming that B_j has occurred.

By its nature, I between arbitrary variables X and Y does not contain directional information. In other words, I does not show causality between X and Y, although it is possible to detect causality between X and Y by the calculation of I using X_L instead of X. X_L is the time series which lags X by L [32]. That is, I between $SS(k)$ and $PS(k+L)$, which is denoted as $I(L)$, shows how much time lag or lead there is between physiological and psychological state changes. $I(L)$ was calculated under lag time set from $L = -2$ to 2 min.

To determine the value of the threshold Tr in equation (2), an assessment function $H(Tr)$ is defined as follows:

$$H(Tr) = \max_{-2 \leqslant L \leqslant 2} I(L) \tag{4}$$

For each subject, the value of Tr was selected to maximize $H(Tr)$ in the range from $Tr = 0.01$ to 0.15.

In this study, the subjective score obtained from the joystick input was chosen as $SS(k)$. Meanwhile, time series of ρ_{max} using PTT, RSA, HRV and LF_{HRV} were chosen as $PS(k)$.

In order to obtain time series of these parameters, beat-to-beat data of HRV and PTT were first calculated. The HRV was calculated from the reciprocal of the inter-R-wave interval of ECG signal and the PTT was defined as the interval from the peak of ECG, R-wave, to the point at which PPG signal begins to rise. And then, at a given time k (min), $\rho_{max}(k)$ was calculated based on the HRV and the PTT observed in the interval between $k-1$ and k (min). A detailed description of the calculation method of ρ_{max} is provided in Ref. [5]. Similarly, $HRV(k)$, $LF_{HRV}(k)$ and $RSA(k)$ were calculated as the mean value, the low-frequency power (0.05–0.15 Hz) and the high-frequency power (0.15–0.45 Hz) of HRV, respectively, in the same interval as described above.

3. Results

Fig. 5 shows the results of the SSQ completed by the subjects before and after the experiment. In these results, all SSQ scores increased significantly ($p < 0.01$, paired t-test) after watching the video and got closer to those obtained from the subjects who were suffered from cyber sickness or simulator sickness [14,23]. Therefore, the moving images included in the video are considered to have induced VIMS.

Fig. 6b shows the changes in ρ_{max} and SS of a subject. SS increased at 11, 15, 20, 24 and 26 min, while ρ_{max} decreased at approximately the same points of time (except for the 24 min point). Fig. 6c shows the average mutual information I between SS and ρ_{max} of this subject. In this figure, I at $L = 0$ min was higher than those observed at the other lag times. This result indicates that the subject's physiological state changed at approximately the same time a VIMS sensation was experienced.

From Fig. 6c, I had a value of 0.3 at $L = 0$. However, the meaning of this value is unclear. Therefore, a computer simulation was carried out to investigate the relationship between I and the concor-

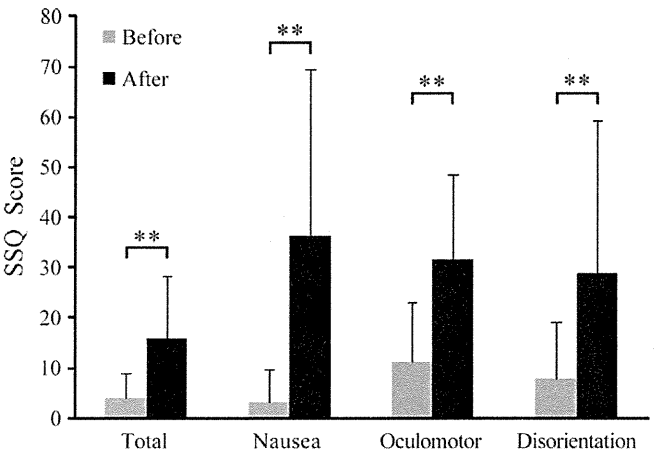

Fig. 5. SSQ scores obtained from subjects before and after watching the video. $^{**}p < 0.01$, paired t-test.

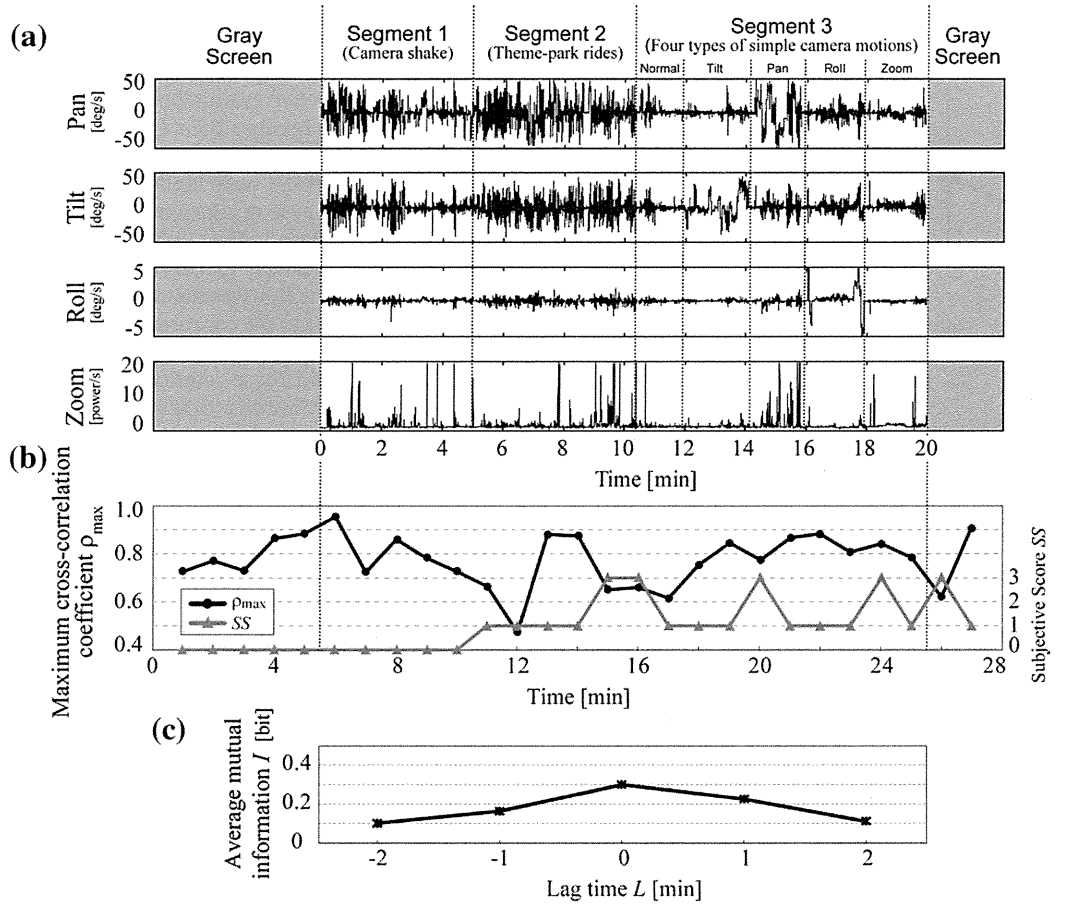

Fig. 6. (a) The global motion vectors of the self-produced video, (b) changes in ρ_{max} (black line) and *SS* (gray line) of a subject, and (c) average mutual information *I* between the *SS* and the ρ_{max}.

dance rate p_c of changing patterns of two temporal sequences resembling $SS(k)$ and $PS(k)$. In the simulation, these temporal sequences changed in the same direction at a rate of p_c (%) and did so in random directions at a rate of $100 - p_c$ (%).

Fig. 7 shows the simulation results. The curve shown in the figure was obtained from a simulation that was performed 1000 times. It can be seen that *I* had a minimum value when p_c was about 33%. This is because there were only three events defined by the difference in the changing pattern of temporal sequences, as shown in Eqs. (1) and (2). Therefore, even if changes to these temporal sequences are perfectly random and there is no statistical dependence between them, they change in the same direction, at a minimum, 33% of the time. This result implies that it is meaningless to compare the values of *I* which are lower than 0.15. In addition, there was a tendency in *I* to increase as p_c decreases when p_c was lower than 33%. This is because the occurrence of two temporal sequences whose changing patterns are significantly different to each other is extremely unlikely to be coincidental.

Fig. 8 shows the mean values of *I* between *SS* and ρ_{max}. These values were calculated as the mean of all test subjects with respect to each lag time between $L = -2$ and 2 min. The values of *I* at $L = -2$ and 2 min showed a lower level than those at the other lag times. However, the standard deviation of *I*, which means individual differences, was high for all lag times. In Fig. 9, relationships between lag time and *I* were plotted for all the subjects whose *I* were the highest at $L = -1$ or 1, hereinafter referred to as $L_{max} = -1$ or 1, respectively. As shown in this figure, there is a possibility that each subject has his/her specific L_{max} because there is only one peak in *I* of each subject for all lag times. And the values of *I* were less than

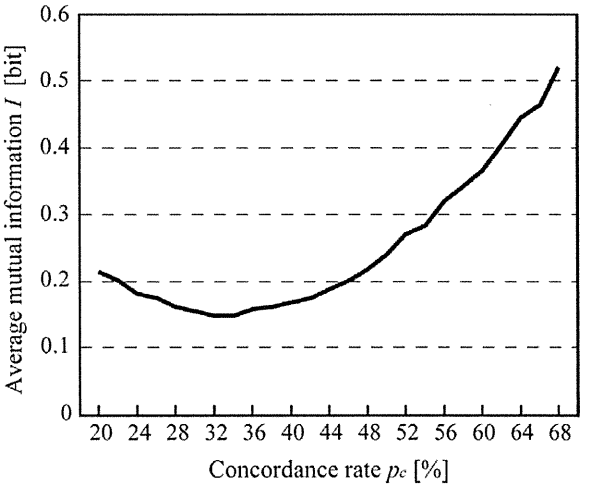

Fig. 7. Relationship between average mutual information *I* and the concordance rate p_c of changes in temporal sequences resembling $SS(k)$ and $PS(k)$. This is the simulation result.

0.2 at other lag times than L_{max}, which indicates there is no statistical dependence between *PS* and *SS*. Thus, for example, if the number of subjects whose L_{max} were -1 increases, the mean value of *I* at $L = 1$ will be relatively low.

To investigate not only the distribution but also the mean value of *I* for subjects with different L_{max}, the mean value of *I* at a lag time L_0 was only calculated for subjects whose L_{max} were L_0. For exam-

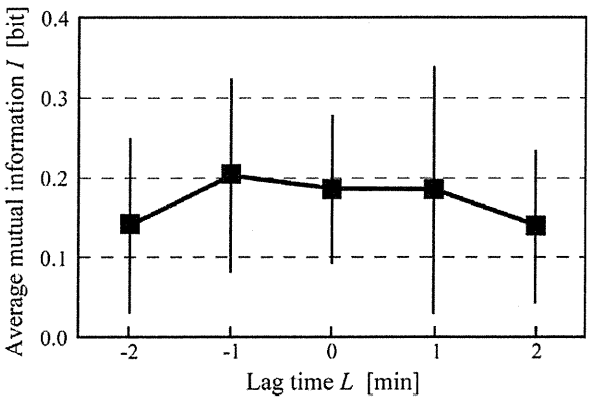

Fig. 8. The mean values of the average mutual information I between *SS* and ρ_{max}. These values were calculated as the mean of all the subjects with respect to each lag time between $L = -2$ and 2 min.

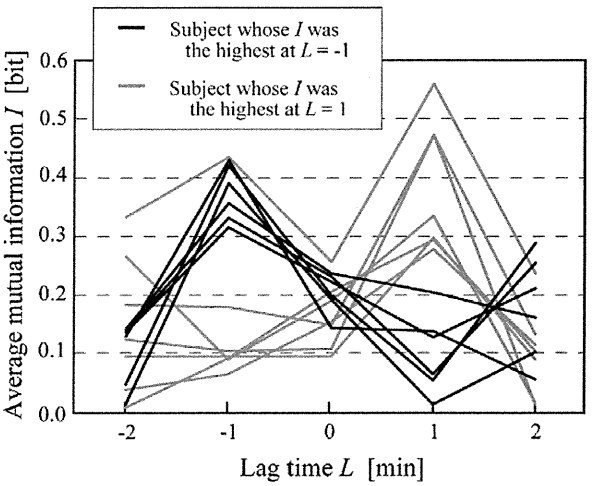

Fig. 9. The average mutual information I between *SS* and ρ_{max} of individual subjects whose I was the highest at $L = -1$ (black line) or $L = 1$ (gray line).

ple, the mean value of I at $L = -1$ was only calculated for six subjects whose I was the highest at $L = -1$ for all lag times.

Fig. 10 shows relationships between lag time L and the mean values of I calculated from four physiological indices: (a) ρ_{max}, (b) *RSA*, (c) *HRV* and (d) LF_{HRV}. These mean values run from 0.1 through 0.4. Also, as shown in Fig. 10a, the values of I obtained from ρ_{max} were higher and standard deviations were lower compared to the results shown in Fig. 8.

In Fig. 10a, I of ρ_{max} was relatively high both at $L = -1$ and 1 and the standard deviation was small, especially at $L = -1$. Additionally, the values of I for *HRV* and LF_{HRV} were lower than that of ρ_{max} on the whole, as shown in Fig. 10c and d. In contrast, for *RSA* shown in Fig. 10b, I was relatively high and the standard deviation was small at $L = 0$.

The statistical significances of the mean values of I among lag times were tested by one-way ANOVA for ρ_{max}, *RSA*, *HRV* and LF_{HRV}. However, no significant difference was found, except for LF_{HRV}. Significant differences were found in the values of I for LF_{HRV} between $L = -2$ and -1, and between $L = -1$ and 1 ($p < 0.05$, Tukey–Kramer test).

4. Discussion

As mentioned in the Methods section, data from six subjects whose subjective scores, *SS*, were zero through the video were excluded from the analysis. The equation of AMI, equation (3), implies that $I(L)$ is always zero for any lag time L if all *SS* are zero. This means that it is impossible to know the temporal relationship between the subjective evaluation scores and physiological indices of the six subjects because their L_{max} are indeterminate.

From Fig. 10, it can be seen that the values of I that were obtained for ρ_{max} and *RSA* were higher than those for the other physiological indices. These results agree with other studies that show that changes in these indices had a relationship to the development of motion sickness [3,5,18,19,17]. The mean value of I obtained for ρ_{max} and *RSA* was about 0.4 at a maximum. This value is nearly equivalent to the concordance rate of 60% in the computer simulation result shown in Fig. 7 and indicates that the changes in the *SS* patterns and these physiological indices corresponded to each other two out of three times on average.

Furthermore, the values of I obtained for ρ_{max} and *RSA* were relatively higher at $L = \pm 1$ and $L = 0$, respectively, than at the other lag times. This result indicates that there was not much difference between the times the subjects experience VIMS symptoms and the times when their physiological state change. However, this tendency was not significant. This result may be caused by the limited number of subjects used to calculate the mean value of I for each lag time, which was approximately five or less, because there were significant individual differences in L_{max}. On the other hand, it is interesting to investigate the relationship between L_{max} and individual characteristics such as gender and age. Accordingly, data from more subjects is needed to make a statistically significant analysis for these relationships.

As shown in Fig. 10c, the maximum point of I obtained for *HRV* was not as high as those obtained for ρ_{max} or *RSA*. This result implies that indices obtained by the frequency or the correlated analysis of *HRV* can reflect the influence of VIMS on nervous activity more than *HRV* itself. On the other hand, the value of I obtained for LF_{HRV} was the lowest of all the $PS(k)$, and this result is considered to be reasonable because it is not clear whether LF_{HRV} reflect the development of VIMS. The difference between LF_{HRV} and *RSA* is considered to be associated with the difference in the autonomic nerve activity linked to these indices. Thus, *RSA* reflects parasympathetic nerve activity while LF_{HRV} is related to both sympathetic and parasympathetic nerve activities [33–35].

There was a minor difference in timing between ρ_{max} and *RSA* when the connection between *SS* and these physiological indices was strengthened. That is, the physiological reaction seen in *RSA* appeared at almost the same time the subjectivity evaluation changed, while the reaction in ρ_{max} appeared before or after the subjectivity evaluation changed, as shown in Figs. 9 and 10a. This latter result is of particular interest because it indicates that there were two types of subjects, whose reaction patterns of ρ_{max} differed from each other. In one type, the physiological states changed prior to the development of VIMS symptoms, while in the other type, the opposite was true. In the former case, the subjects had watched a scene which had the potential to induce VIMS and experienced changes to their physiological states. Then, approximately 1 min later, their emotional states changed. In the latter case, the possibility exists that the physiological states of the subjects changed as a result of the discomfort induced by VIMS. In this matter, the proposed method revealed that there were significant differences in the temporal relationship between physiological and emotional states among individuals.

In this study, it was necessary to establish a method to investigate not only the distribution of lag times but also the strength of the relationship between physiological and emotional states of subjects watching a video in considering their individual differences. The proposed method is considered to be an effective approach to accomplish our purpose. However, the values of I were not so high, which were less than 0.6, and no significant difference

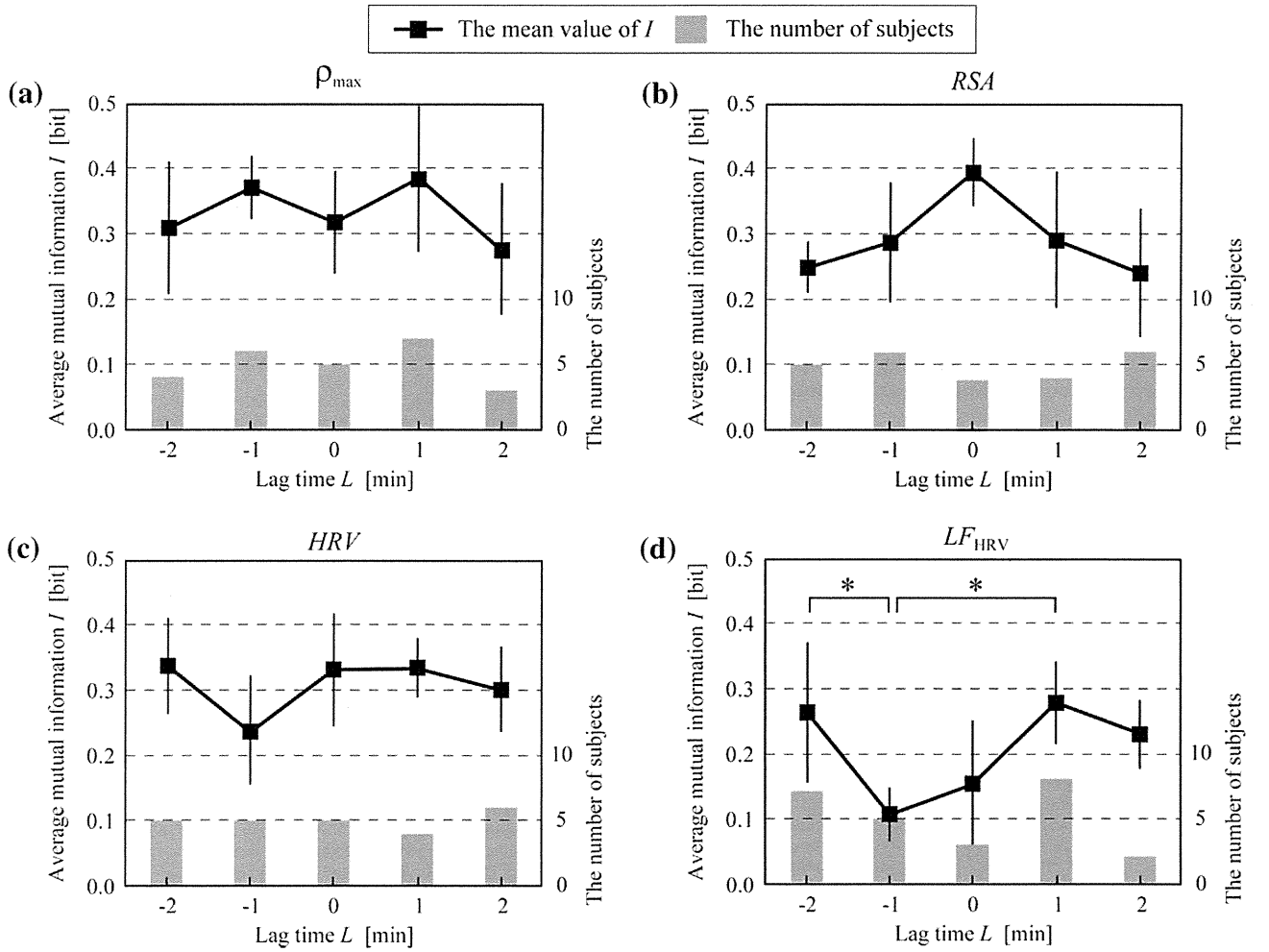

Fig. 10. The mean values of I between *SS* and four physiological indices: (a) ρ_{max}, (b) *HRV*, (c) LF_{HRV}, and (d) *RSA*. The bar graph at each lag time represents the number of subjects whose I was the highest at that lag time. $^{*}p < 0.05$, Tukey–Kramer test.

was found in the mean value of I between lag times for most physiological indices used in this study.

On the other hand, there is still room for improvement not only in the physiological indices but also in the subjective assessment method for the calculation of I. For example, by the use of techniques such as neural networks and genetic algorithms [36] with the AMI as a performance function, it may be possible to create a new index that can detect the development of VIMS with high accuracy. The continuous subjective assessment, in which subjects can report *SS* whenever they experience VIMS symptoms, may be useful to improve the proposed method. In the experiment of this study, the subjects reported *SS* by moving a joystick every time they heard a buzzer sound at 1 min intervals. This assessment method was designed to make certain subjects report their symptoms at least once a minute, however, there is a possibility to cause a delay, which is 1 min at worst, between the time subjects experience VIMS symptoms and that they change *SS*. On the other hand, even if the continuous subjective assessment is used, subjects do not always report *SS* just after they experience the symptoms because they may forget to report, and this becomes a serious problem for the calculation of AMI.

Information of video scenes related to VIMS cannot be obtained directly from the values of I nor L_{max}. As a first step to detect these scenes, it is necessary to find a physiological index that well reflects VIMS symptoms by calculating AMI as mentioned above. Then, it will be possible to find out which scenes in a video are associated with the onset of VIMS by analyzing the physiological index of subjects watching the video. In addition, if the physiological index has a tendency to change prior to feeling VIMS symptoms, it may be possible to predict the development of VIMS.

5. Conclusion

In this study, the AMI was employed to investigate the temporal relationship between subjective evaluation scores and collected physiological indices. Our analysis of experimental data suggested that changes in certain physiological indices showed a concordance rate of more than 60% with the change in the severity of VIMS symptoms. This result indicates that it may be possible to detect video scenes that are likely to induce VIMS by analyzing physiological indices. Furthermore, the physiological states of some test subjects changed prior to the development of VIMS symptoms, even though there were significant individual differences in the temporal relationship. An analysis of the temporal relationship between the physiological states and the cognitive levels of test subjects suffering from VIMS is expected to shed light on the pathogenesis of VIMS.

In our future work, analysis using other physiological indices, such as gastric tachyarrhythmia, which has frequently been reported as having a relationship with motion sickness, will be necessary. And our method using AMI should be compared to the

other techniques such as Cronbach's Alpha [37], which is a form of factor analysis. Furthermore, the number of sampling points used in this study might be insufficient for a full analysis of the AMI, so an experiment in which the video watching duration is extended, or where more subjects watch the same video repeatedly, should be performed to confirm the validity of the proposed method.

Acknowledgements

Dr. Hiroyasu Ujike and Dr. Atsuhiko Iijima provided excellent technical support in performing the experiment.

This study was subsidized by JKA through its Promotion funds from KEIRIN RACE and was supported by the Mechanical Social Systems Foundation and the Ministry of Economy, Trade and Industry of Japan.

References

[1] J.T. Reason, Motion sickness: some theoretical and practical considerations, Applied Ergonomics 9 (3) (1978) 163–167.
[2] N. Himi, T. Koga, E. Nakamura, M. Kobashi, M. Yamane, K. Tsujioka, Differences in autonomic responses between subjects with and without nausea while watching an irregularly oscillating video, Autonomic Neuroscience. Basic and Clinical 116 (2004) 46–53.
[3] N. Sugita, M. Yoshizawa, A. Tanaka, K. Abe, T. Yambe, S. Nitta, Evaluation of the effect of visual stimulation on humans by simultaneous experiment with multiple subjects, in: Proceedings of the 27th Annual International Conference of the IEEE Engineering in Medicine and Biology Society, 2005 (CD-ROM).
[4] N. Sugita, M. Yoshizawa, M. Abe, A. Tanaka, T. Yambe, S. Nitta, S. Chiba, Biphasic effect of visually-induced motion sickness revealed by time-varying correlation of autonomic nervous system, in: Proceedings of the tenth International Conference on Human – Computer Interaction, 2005 (CD-ROM).
[5] N. Sugita, M. Yoshizawa, M. Abe, A. Tanaka, T. Watanabe, S. Chiba, T. Yambe, S. Nitta, Evaluation of adaptation to visually induced motion sickness based on the maximum cross-correlation between pulse transmission time and heart rate, vol. 4(37), Journal of NeuroEngineering Rehabilitation (Online), 2007, <http://www.jneuroengrehab.com/content /4/1/35>.
[6] H. Ujike, K. Ukai, K. Nihei, Survey on motion sickness-like symptoms provoked by viewing a video movie during junior high school class, Displays 29 (2) (2008) 81–89.
[7] M. Emoto, M. Sugawara, Y. Nojiri, Viewing angle dependency of visually-induced motion sickness in viewing wide-field images by subjective and autonomic nervous indices, Displays 29 (2) (2008) 90–99.
[8] N. Sugita, M. Yoshizawa, A. Tanaka, K. Abe, S. Chiba, T. Yambe, S. Nitta, Quantitative evaluation of effects of visually-induced motion sickness based on causal coherence functions between blood pressure and heart rate, Displays 29 (2) (2008) 167–175.
[9] J.E. Bos, S.C. Vries, M.L. Emmerik, E.L. Groen, The effect of internal and external fields of view on visually induced motion sickness, Applied Ergonomics 41 (4) (2010) 516–521.
[10] J.T. Reason, J.J. Brand, Motion Sickness, Academic Press, London, 1975.
[11] J.T. Reason, Motion sickness adaptation: a neural mismatch model, Journal of the Royal Society of Medicine 71 (1975) 819–829.
[12] A.J. Benson, Motion sickness, in: M.R. Dix, J.S. Hood (Eds.), Vertigo, Wiley, New York, 1984, pp. 391–426.
[13] R.S. Kennedy, N.E. Lane, K.S. Berbaum, M.G. Lilienthal, Simulation sickness questionnaire: an enhanced method for quantifying simulator sickness, International Journal of Aviation Psychology 3 (3) (1993) 203–220.
[14] W.T. Lo, R.H.Y. So, Cybersickness in the presence of scene rotational movements along different axes, Applied Ergonomics 32 (1) (2001) 1–14.
[15] S. Nichols, H. Patel, Health and safety implications of virtual reality: a review of empirical evidence, Applied Ergonomics 33 (3) (2002) 251–271.
[16] S. Sharples, S. Cobb, A. Moody, J.R. Wilson, Virtual reality induced symptoms and effects (VRISE): comparison of head mounted display (HMD), desktop and projection display systems, Displays 29 (2) (2008) 58–69.
[17] R.S. Kennedy, J. Drexler, R.C. Kennedy, Research in visually induced motion sickness, Applied Ergonomics 40 (2010) 494–503.
[18] S.H.J. Uijtdehaage, R.M. Stern, K.L. Koch, Effects of eating on vection-induced motion sickness, cardiac vagal tone, and gastric myoelectric activity, Psychophysiology 29 (1992) 193–201.
[19] P.J. Gianaros, K.S. Quigley, E.R. Muth, M.E. Levine, R.C. Vasko Jr., R.M. Stern, Relationship between temporal changes in cardiac parasympathetic activity and motion sickness severity, Psychophysiology 40 (2003) 39–44.
[20] S. Hu, W.F. Grant, R.M. Stern, K.L. Koch, Motion sickness severity and physiological correlates during repeated exposures to a rotating optokineic drum, Aviation, Space, and Environmental Medicine 62 (1991) 308–314.
[21] J.C. Miller, T.J. Sharkey, G.A. Graham, M.E. McCauley, Autonomic physiological data associated with simulator discomfort, Aviation, Space, and Environmental Medicine 64 (9) (1993) 813–819.
[22] R.M. Stern, K.L. Koch, H.W. Leibowitz, I.M. Lindblad, C.L. Shupert, W.R. Stewart, Tachygastria and motion sickness, Aviation, Space, and Environmental Medicine 56 (1985) 1074–1077.
[23] B. Min, S. Chung, Y. Min, K. Sakamoto, Psychophysiological evaluation of simulator sickness evoked by a graphic simulator, Applied Ergonomics 35 (2004) 549–556.
[24] S. Cerutti, G. Baselli, A. Bianchi, M.G. Signorini, Spectral techniques of analysis for blood pressure and heart rate signals, Blood Pressure and Heart Rate Variability, IOS Press, Amsterdam, 1992.
[25] M. Pagani, L. Federico, G. Stefano, R. Ornella, F. Raffaellow, P. Paolo, S. Giulia, M. Gabriella, Power spectral analysis of heart rate and arterial pressure variabilities as a marker of sympatho–vagal interaction in man and conscious dog, Circulation Research 59 (1986) 178–193.
[26] G.B. Guo, M.D. Thames, F.M. Abboud, Arterial baroreflexes in renal hypertensive rabbits, Circulation Research 53 (1983) 223–234.
[27] T. Matsukawa, E. Gotoh, O. Hasegawa, H. Shionoiri, O. Tochikubo, M. Ishii, Reduced baroreflex changes in muscle sympathetic nerve activity during blood pressure elevation in essential hypertension, Journal of Hypertens 9 (1991) 537–542.
[28] S. Ogoh, J.P. Fisher, E.A. Dawson, M.J. White, N.H. Secher, P.B. Raven, Autonomic nervous system influence on arterial baroreflex control of heart rate during exercise in humans, Journal of Physiology 556 (2) (2005) 599–611.
[29] B. Gribbin, A. Steptoe, P. Sleight, Pulse wave velocity as a measure of blood pressure change, Psychophysiology 13 (1) (1976) 86–90.
[30] K. Jinzenji, H. Watanabe, N. Kobayashi, Global Motion Estimation for Sprite Production and Application to Video Coding (in Japanese), Information and Communication Engineers J83-D-II (2) (2000) 535–544.
[31] C.E. Shannon, The mathematical theory of communicaton, Bell System Technical Journal 27 (1948) 379–423.
[32] N. Tanaka, H. Okamoto, M. Naito, Detecting and evaluating intrinsic nonlinearity present in the mutual dependence between two variables, Physica D 147 (2000) 1–11.
[33] A. Malliani, M. Pagani, F. Lombardi, S. Cerutti, Cardiovascular neural regulation explored in the frequency domain, Circulation 84 (2) (1991) 482–492.
[34] G.G. Berntson, J.T. Bigger, D.L. Eckberg, P. Grossman, P.G. Kaufmann, M. Malik, H.N. Nagaraja, S.W. Porges, J.P. Saul, P.H. Stone, M.W. van derMolen, Heart rate variability: origins, methods, and interpretive caveats, Psychophysiology 34 (1997) 623–648.
[35] A. Malliani, N. Montaro, Heart rate variability as a clinical tool, Italian Heart Journal 3 (2002) 439–445.
[36] J.H. Holland, Adaptation in Natural and Artificial Systems: An Introductory Analysis with Applications to Biology, Control, and Artificial Intelligence, MIT Press, 1975.
[37] L.J. Cronbach, Coefficient alpha and the internal structure of tests, Psychometrika 16 (3) (1951) 297–334.

Journal of Biomechanical Science and Engineering
Vol. 6, No. 4, 2011

Numerical Analysis of One-dimensional Mathematical Model of Blood Flow to Reproduce Fundamental Pulse Wave Measurement for Scientific Verification of Pulse Diagnosis*

Atsushi SHIRAI**, Tsutomu NAKANISHI** and Toshiyuki HAYASE**
**Institute of Fluid Science, Tohoku University,
2-1-1, Katahira, Aoba-ku, Sendai 980-8577, Japan
E-mail: shirai@ifs.tohoku.ac.jp

Abstract

Pulse diagnosis in traditional Chinese medicine is said to be able to detect not only illness but also decline of health in the patients from tactile sense of the pulse in the radial artery at the wrists. This diagnosis, however, is not supported by concrete scientific evidence. The authors have proposed a non-linear spring model of subcutaneous tissue on the radial artery and one-dimensional arterial blood flow model in an arm for the purpose of scientific verification of the pulse diagnosis. They performed, in the former study, a numerical experiment with this mathematical model in which the radial artery was indented in a stepwise manner by a pressure sensor, which extract the fundamental mechanism of the pulse diagnosis, to validate the subcutaneous tissue model and to find the appropriate coefficient to fit the experimental result. They investigated, in this research, contribution of parameters of supply pressure of the blood and tube law of the artery on the change in the pressure pulse waves with the indentation steps with respect to mean value P_{oav} and amplitude ΔP_o of the pressure. It was shown that mean supply pressure affects both P_{oav} and ΔP_o, while amplitude of the supply pressure affects ΔP_o. It was also shown that profile of ΔP_o vs. distance of the indentation changes drastically as the artery becomes hard. Lastly, it was examined to reproduce the experimentally obtained pressure pulse waves during the indentation in their former work with the mathematical model by adjusting the parameters. The result showed better agreement than the former result, but it implied that ulnar artery had to be taken into consideration for quantitative fitting of the pulse waves to the range where the radial artery was nearly flattened by the indentation.

Key words: Pulse Diagnosis, Pressure Wave, Mathematical Model, Numerical Simulation, One-Dimensional Analysis

1. Introduction

Integrated medicine (IM) that combines complementary and alternative medicine (CAM), such as traditional Chinese medicine, Ayurveda or aromatherapy, with modern Western medicine has recently attracted our attention. Research on IM is being carried out with the expectation of health maintenance, a decrease of medical expenses by prevention, early stage detection of diseases and perfect recovery from disease. It is hoped that

*Received 14 Jan., 2011 (No. 11-0034)
[DOI: 10.1299/jbse.6.330]

custom-made medical treatment based on individual patients' conditions can be realized.

Traditional Chinese medicine, represented by herbal medicine, acupuncture or moxibustion, is a well-known CAM. Pulse diagnosis is also a traditional Chinese medical technique. In the pulse diagnosis, a doctor places his fingers at both wrists of a patient to indent the radial arteries with various indentation patterns and diagnoses his/her diseases from the tactile sense of the pulse detected by the fingers. This is a simple and non-invasive technique and is said to be able to diagnose not only the diseases but also the patient's physical condition or presence of latent disease. The pulse diagnosis has been established with accumulated experiences of the doctors, and thus, neither scientific evidence of the diagnosis nor rigorous quantitative guideline for the diagnosis exist but qualitative image of tactile sense of the pulse waves specific to diseases. So, various researches have been performed on the objectification of the diagnosis[(1)-(5)]. In those researches, the pulse waves of the patients were measured by an applanation tonometry or a photoelectro-plethysmograph focusing on finding significant characteristics on the pulse waves for a specific disease and giving interpretation on them from medical point of view, but mechanism of the pulse diagnosis, i.e. cause-and-effect relationship between diseases and change in the waveform, was left unknown. This is an issue in integrating the pulse diagnosis to the modern Western medicine. Then, numerical simulation is a powerful tool for the fundamental understanding of the mechanism and analytical verification of the pulse diagnosis, because the mathematical model is grounded on rigorous physical laws.

Since blood flow is pulsatile by the heartbeat, some change in the circuit theoretically appears on the waveform of the pulsation by considering the blood circulatory system as a hydraulic circuit. For example, Konno et al.[(6)] examined the change of the waveform in their experimental research on the pulsatile flow in a closed circuit. For the investigation of the propagation or reflection of the pressure pulse waves, mathematical models of arterial vasculature have been proposed and numerical simulations have been performed[(7)-(10)]. In those researches, blood flow was expressed in one dimension, and the blood flow and the propagation of the pressure waves were solved simultaneously with deformation of the vessels under the physiological condition. The artery, however, has to be indented to reproduce the pulse diagnosis, because the authors have expected that essence of the diagnosis is in the change in the pulse waves by the indentation. For this purpose, we have to take into consideration the subcutaneous tissue between the radial artery and the finger. The authors proposed a non-linear spring model of subcutaneous tissue on the radial artery and one-dimensional blood flow in the artery of an arm to reproduce indentation of the radial artery by a finger[(11)]. They also developed an experimental setup to press down a pressure sensor against the radial artery at the wrist, and performed an experiment in which the radial artery was indented stepwise by a pressure sensor, which extracted the fundamental mechanism of the pulse diagnosis, to measure the change in the pressure pulse waves with the indentation steps. Quantitative agreement of the numerical and the experimental results is a necessary condition for the numerical reproduction of the pulse diagnosis and further investigation on the diagnosis. They then numerically reproduced the indentation experiment with the mathematical model to validate the subcutaneous tissue model and to find the appropriate parameter to fit the experimental result, and concluded that supply pressure and physical characteristics of the artery had to be adjusted for the quantitative agreement.

Therefore, in the present paper, the authors performed the numerical experiment to examine the contribution of the parameters of supply pressure of the blood and tube law of the artery to the change in the pressure pulse waves with the indentation steps with respect to the mean value and amplitude of the pressure, and lastly to verify their contribution to the pressure pulse waves detected by the sensor, parameters were adjusted to fit the numerical result with the experimental result.

Nomenclatures

$A(x)$: Cross-sectional area of artery at axial position x [m^2]
$A_0(x)$: Cross-sectional area of artery at axial position x at ϕ = 13.3 kPa [m^2]
$A_C(x)$: Cross-sectional area of artery at the inflection point of the tube law [m^2]
C_v: Capacitance of venous system [m^3/Pa]
$D(x)$: Peripheral length of artery at axial position x [m]
dy: Local displacement of arterial wall under pressure sensor [m]
dy_a: Time-averaged displacement of arterial wall under the center of pressure sensor [m]
dy_{av}: Mean displacement of arterial wall under pressure sensor [m]
f_t: Resistance coefficient of artery (= $\lambda/4$)
$P(x)$: Inner pressure of artery at axial position x [Pa]
P_E: Pressure at downstream end of artery [Pa]
$P_e(x)$: External pressure of artery at axial position x [Pa]
P_o: Pressure measured by pressure sensor [Pa]
P_{sav}: Mean supply pressure [Pa]
ΔP_o: Amplitude of pulsation pressure [Pa]
ΔP_s: Amplitude of supply pressure [Pa]
P_{ra}: Pressure in right atrium [Pa]
P_v: Venous pressure [Pa]
$Q(x)$: Flow rate of blood in artery at axial position x (= $A(x)u(x)$) [m^3/s]
Q_d: Flow rate of blood at downstream end of artery [m^3/s]
Q_{vi}: Flow rate of blood into vein [m^3/s]
Q_{vo}: Flow rate of blood out of vein [m^3/s]
$Re_x(x)$: Local Reynolds number in artery at axial position x (= $u(x)(A(x)/w(x))/\nu$)
R_m: Flow resistance in microvasculature [Pa·s/m^3]
R_v: Flow resistance in vein [Pa·s/m^3]
T: Tension of arterial wall in axial direction [N/m]
t: Time [s]
Δt: Time step for computation [s]
$u(x)$: Mean flow velocity of blood in artery at axial position x [m^3/s]
$w(x)$: Width of artery at axial position x when its cross section is assumed to be rectangle [m]
x: Axial position of artery from its upstream end [m]
Y: Displacement of pressure sensor [m]
$y(x)$: Height of artery from its center at axial position x when its cross section is assumed to be rectangle [m]
γ: Damping coefficient to the change in cross-sectional area of artery [Pa·s/m^2]
λ: Friction coefficient of pipe
ν: Kinematic viscosity of blood [m^2/s]
ρ: Density of blood [kg/m^3]
ϕ: Tube law [Pa]
ϕ_0: Transmural pressure (= $P - P_e$) at A/A_0 = 1 [Pa]

2. Method

In this section, measurement of pressure pulse waves by a pressure sensor and mathematical model to numerically reproduce the measurement are briefly explained. See Refs. (3) and (11) for the details.

2.1 Measurement of Pressure Pulse Waves by Pressure Sensor

Figure 1 shows the experimental setup for the measurement of pressure pulse waves in the radial artery at the wrist[11]. The pressure sensor moves vertically by the screw to indent

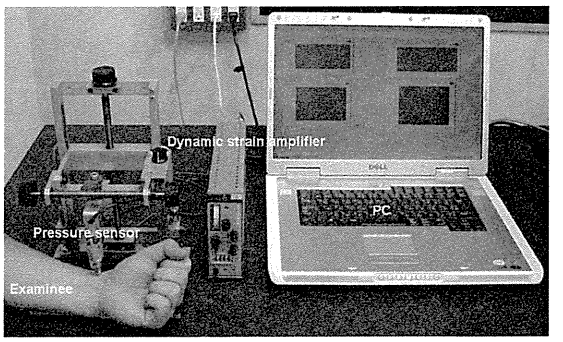

Fig. 1 Experimental setup for measurement of pulse waves[11].

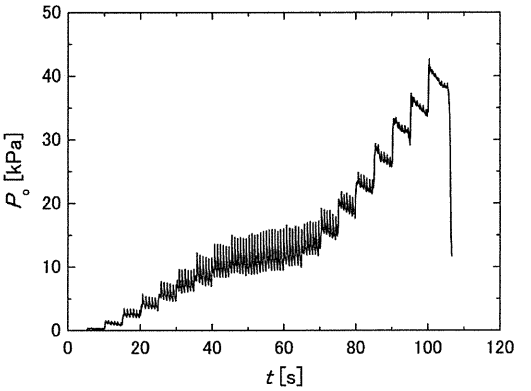

Fig. 2 Measured pressure waves P_o during the indentation[11].

the radial artery. The signal from the sensor was stored in a PC via a low-pass filter of 1 kHz of the strain amplifier and an A/D converter.

In the experiment, the pressure sensor was set at the position where pulsation was detected most clearly on the radial artery of a healthy 24 y.o. male volunteer, and measurement of the pulse waves was performed by the following steps, following the ethics regulation of Tohoku University and under the supervision of a medical doctor;

1: Displacement of the pressure sensor Y is set to 0 mm at the point the sensor touches wrist of the volunteer:

2: Press the sensor 0.5 mm down on the wrist and hold for 5 s to measure the pressure pulse waves.

3: Repeat step #2 until Y reaches 10 mm or the volunteer feels pain.

Figure 2 shows an example of the measured pressure pulse waves P_o. Here, each indentation period is not exactly 5 s because the screw was rotated by hand for the safety of the volunteer. The mean value of P_o in each indentation step correlates with physical characteristics of skin, subcutaneous tissue, blood vessel and mean blood pressure. Amplitude of the pulsation of P_o correlates with the pulsation of the blood flow. The mean value of P_o denoted as P_{oav} in the following has a non-linear profile with respect to indentation having an inflection point. The amplitude denoted as ΔP_o has the maximum around the inflection point of P_{oav}. This profile matches the principle of the applanation tonometry[12]. That is, pressure pulse waves in a cylindrical blood vessel that propagate outward are the balance of the inner pressure and radial projection of circumferential tension of the vessel wall. When the blood vessel is pressed between two flat surfaces, the circumferential tension can be ignored in the flattened area for the pulsatile inner pressure to directly propagate through that area. If the vessel is pressed more, blood flow itself ceases and the pulsation disappears. In this figure, pulsation of the blood flow is still observed in the range of $t \geq 100$ s where Y reaches 10.0 mm. This implies that the blood

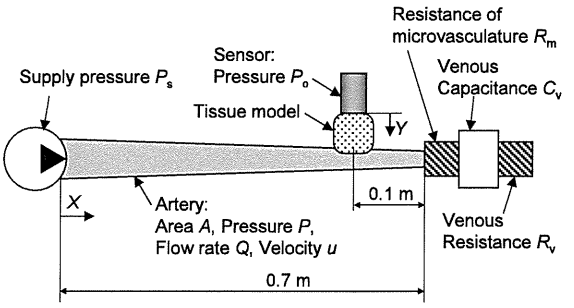

Fig. 3 Schematic of mathematical model.

flow was not fully ceased by the pressure sensor. The data shown in Fig. 2 is used for the comparison with the numerical results in the following.

2.2 Mathematical Model of Measurement of Pressure Pulse waves

Figure 3 shows a schematic of the mathematical model. This model is based on the collapsible tube model derived by Hayashi et al.[13]. In this research, we treated the series of subclavian artery, axillary artery, brachial artery and radial artery, neglecting the ulnar artery for the sake of simplicity. The arteries were assumed to be a tapered collapsible tube with a length of 700 mm. The inlet radius of the collapsible tube was 4.23 mm and the outlet radius was 1.74 mm, corresponding to those of the subclavian and radial arteries, respectively[14]. The linear resistance of the microvasculature, and the venous capacitance and the resistance of the Windkessel model were connected to the downstream end of the artery.

Blood was considered to be an incompressible Newtonian fluid with a density ρ of 1,050 kg/m^3 [15] and a kinematic viscosity ν of 3.8×10^{-6} m^2/s [16]. One-dimensional equation of momentum and continuity of blood in the artery are expressed as follows[13]:

$$\frac{1}{A}\frac{\partial Q}{\partial t}-\frac{Q}{A^2}\frac{\partial A}{\partial t}+\frac{Q}{A^2}\frac{\partial Q}{\partial x}-\frac{Q^2}{A^3}\frac{\partial A}{\partial x}=-\frac{1}{\rho}\frac{\partial P}{\partial x}-\frac{1}{2}f_t\frac{Q|Q|}{A^3}D, \tag{1}$$

$$\frac{\partial A}{\partial t}+\frac{\partial Q}{\partial x}=0. \tag{2}$$

where drag coefficient f_t is given as follows by the local Reynolsd number Re_x:

$$f_t=\frac{\lambda}{4}=\begin{cases}16/Re_x & (Re_x\le 1{,}067)\\ 0.015 & (Re_x>1{,}067)\end{cases}. \tag{3}$$

Here, friction coefficient λ of a pipe with a rough surface was $64/Re_x$ for the laminar flow region and was approximated by 0.06 in the turbulent flow region for the sake of simplicity[17].

To describe deformation of the collapsible tube, the initial cross section of the tapered collapsible tube was assumed to be a square whose cross-sectional area was same as that of the tube at all axial positions, i.e., both height y and width w of the tube were 7.50 mm at the inlet and 3.08 mm at the outlet. The width w was fixed along the collapsible tube and only the height y was changed to describe the deformation of the tube. Cross-sectional area A of the tube at arbitrary axial position x was expressed as A_0 when transmural pressure P–P_e was 13.3 kPa[18]. Force equilibrium acting on the tube wall in the normal direction to the wall was expressed as[13]

$$T\frac{\partial^2 y}{\partial x^2}=P_e-P+\phi\left(\frac{A}{A_0}\right)+\gamma\frac{\partial A}{\partial t}, \tag{4}$$

where T was approximated to be 130 N/m neglecting the variation of the tension, e.g. 107 N/m for the brachial artery and 138 N/m for the radial artery, because the series of the arteries was modeled as a tapered collapsible tube in this research[11].

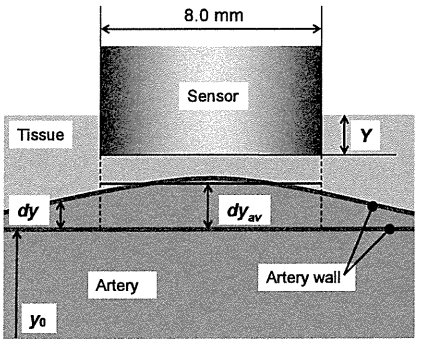

Fig. 4 Schematic of deformation of arterial wall and compression of subcutaneous tissue.

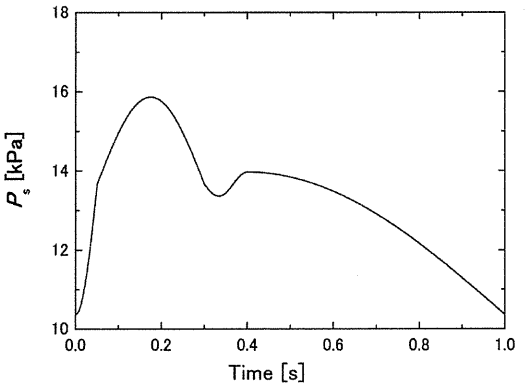

Fig. 5 Waveform of supply pressure P_s.

The third term of the right-hand side of Eq. (4) is the tube law of the artery. The tube law ϕ is the relationship between transmural pressure P–P_e and the cross-sectional area A of the tube to represent stiffness of the blood vessel. The tube law introduced in the former researches on propagation and reflection of the pulse waves was based on the Laplace's law[7]-[10]. This model, as Olufsen mentioned[7], has a property that the area becomes infinite at a finite transmural pressure. In contrast, Shimizu and Ryumae[18] presented a tube law based on experimental data of canine carotid artery and femoral artery, which reproduces stiffening of the artery in the positive transmural pressure range. The authors introduced this model expressed as follows assuming human arteries have qualitatively the similar tendency as the canine arteries:

$$\phi\left(\frac{A}{A_0}\right)=\frac{\phi_0}{1+C_1-C_2}\left[\left(\frac{A}{A_0}\right)^{n_1}+C_1\frac{A}{A_0}-C_2\right] \quad \text{for } \frac{A_c}{A_0}\le\frac{A}{A_0}$$
$$\phi\left(\frac{A}{A_0}\right)=\phi_0\left[C_3\left(\frac{A-A_c}{A_0}\right)^{n_2}+C_4\frac{A-A_c}{A_0}+C_5\right] \quad \text{for } 0<\frac{A}{A_0}\le\frac{A_c}{A_0} \tag{5}$$

where the parameters are as follows: ϕ_0 = 13.3 kPa, C_1 = 0.1 and C_2 = 0.05. The A_C is the cross-sectional area at the connecting point of the two equations of Eq. (5), and C_3, C_4 and C_5 were determined to smoothly connect the two equations and the first differentiation at $A = A_C$. In this research, the gradient of ϕ at A/A_0 = 1.0 was doubled from the original model[18] and the absolute value of transmural pressure at A/A_0 = 0.0 was assumed to be twice of the mean blood pressure13.3 kPa (100 mmHg), considering the fact that Young's moduli of the canine aorta and the human radial artery are 0.43 MPa and 0.8 MPa, respectively[14], [19], and the fact that blood could not be stopped by an external pressure more than three times the mean blood pressure as shown in Fig. 2. Consequently, the parameters were determined as n_1 = 5, n_2 = 6, A_c/A_0 = 0.3, and ϕ = -26.6 kPa at A/A_0 = 0.